atmosphere

Article

Short-Period Variation of the Activity of Atmospheric Turbulence in the MLT Region over Langfang

Zewei Wang [1,2], Cunying Xiao [1,2,*], Xiong Hu [3,4], Junfeng Yang [3,4], Xuan Cheng [3,4], Qingchen Xu [3,4], Luo Xiao [1,2] and Xiaoqi Wu [1,2]

1 Institute for Frontiers in Astronomy and Astrophysics, Beijing Normal University, Beijing 100875, China
2 Department of Astronomy, Beijing Normal University, Beijing 100875, China
3 State Key Laboratory of Space Weather, National Space Science Center, Chinese Academy of Sciences, Beijing 100045, China
4 Key Laboratory of Science and Technology on Environmental Space Situation Awareness, National Space Science Center, Chinese Academy of Sciences, Beijing 100190, China
* Correspondence: xiaocunying@bnu.edu.cn

Abstract: In this paper, we investigate the activity of atmospheric turbulence in the MLT region and the relationship between the activity of atmospheric turbulence and atmospheric wave activity. We use data from the Langfang MF radar (39.4° N, 116.7° E) from July 2019 to June 2020 and NRLMSIS 2.0 to calculate the parameters of atmospheric wave activity and atmospheric turbulence energy dissipation rate (ε). Atmospheric ε is modulated by different periods at different altitudes, and while there are 12 h and 24 h periods at all altitudes, the main period is different at different altitudes. A comparison of the ε with atmospheric tide activity shows that tides have an effect on ε, and the influence of tides on ε may be different at different altitudes. The pattern of variation in ε is similar to that of the atmospheric activity of the gravity wave, with both ε and the atmospheric activity of the gravity wave showing significant semi-annual variation.

Keywords: medium-frequency radar; turbopause; turbulence; MLT region

Citation: Wang, Z.; Xiao, C.; Hu, X.; Yang, J.; Cheng, X.; Xu, Q.; Xiao, L.; Wu, X. Short-Period Variation of the Activity of Atmospheric Turbulence in the MLT Region over Langfang. *Atmosphere* **2023**, *14*, 1045. https://doi.org/10.3390/atmos14061045

Academic Editor: Doris Folini

Received: 18 April 2023
Revised: 23 May 2023
Accepted: 13 June 2023
Published: 17 June 2023

1. Introduction

The mesosphere and lower thermosphere (MLT) region has an altitude of about 50 to 110 km and there is an overlap with the lower ionosphere (60–130 km). This region is subject to a number of dynamical processes that are different from those in the rest of the atmosphere, many of which result in turbulence. Turbulence is a key active factor in the atmosphere and has a significant impact on the thermal structure and on the various types of waves in the atmosphere. Turbulence can transfer their potential and kinetic energy to the molecular scale through cascading processes, and energy is converted to heat through viscous dissipation and thermoconductivity. Furthermore, turbulence also affects wind shear and temperature inversions at about 100 km, as well as the transport of small species.

There have been many studies on the activity of atmospheric turbulence in the MLT region. Lübken [1] observed significant seasonal dependence of the turbulence energy dissipation rate (ε). Sasi et al. [2] also observed that ε shows a seasonal variation, with a dominant summer maximum. Roper et al. [3] observed the diurnal variation of ε at the Bear Lake Observatory (41.9° N, 111.41° E) and Holdsworth et al. [4], using the Buckland Park MF radar (34° N, 138° E), observed the diurnal variation of the turbulent velocity. Focusing on turbopause, where ε has a value of zero, Hall et al. [5,6] found an annual cycle in its position and studied its long-term pattern of variation. Lehmacher et al. [7] examined the relationship between the spatiotemporal variation of the middle atmospheric turbulence and the static stability of the background atmosphere.

Wave breaking is one of the main sources of turbulence, with strong reverse influence. Li et al. [8] estimated the values of the diffusion coefficient and energy dissipation rate of turbulent vortices and investigated their relationship to gravity wave breaking. Roper et al. [9] found the correlation between gravity waves and turbulent velocity is remarkable and suggested that there might be a correlation between the rate of dissipation of turbulent energy and the 24 h component of the mean wind in the meteor region by comparing monthly averages [10]. Strelnikov et al. [11] observed significant tidal modulation in ε. The study of the short-term variability of turbulent activity facilitates the observational search for the relationship between turbulent activity and atmospheric waves.

In this study, we used one year of data provided by the medium frequency (MF) radar at LangFang, China (39.4° N, 116.7° E) to calculate ε and find the height of turbopause. The main objective of this study is to analyze the structure of the activity of turbulence in the mesosphere and lower thermosphere atmosphere and its short-period variation pattern with height, and to study the relationship between ε and atmospheric wave activity.

2. Data and Methods

The Langfang MF radar was installed and began its observations in June 2009. The radar operates at a frequency of 1.99 MHz with a spatial resolution of 2 km and a temporal resolution of 4 min and operates continuously for 24 h. The radar has a pulse repetition rate of 80 Hz and a coherent accumulation of 32 at daytime, and a pulse repetition rate of 40 Hz and a coherent accumulation of 16 at night. A lot of data have been gathered with this radar [12,13], and we use radar data from July 2019 to June 2020.

The radar antenna transmits a narrow vertical beam and the radio waves within the beam are scattered as they propagate until they are completely reflected by the E region of the ionosphere, due to the high electron density. The MF radar senses the field pattern on the ground through spaced receiving antennas. Due to the irregularity of the electron density, there are scatterers with different refractive indices. The time- and space-dependent function of the ground diffraction pattern of a radar echo generated by a scatterer can be expressed as an ellipsoidal function.

Full correlation analysis (FCA) is used to estimate atmospheric wind speed from the surrounding diffraction pattern produced by atmospheric backscattering of the transmission signal with irregular refractive indices. The pattern is typically sampled at three non-collinear locations and the the spatio-temporal correlation function is parameterized using the temporal auto-correlation function and cross-correlation function calculated from the complex signals recorded at these antennas. The velocity of the scatterer's motion can be obtained by measuring the motion of the ground diffraction pattern. The scattered signal is not only influenced by the background wind, but also by the disturbance of the random motion of the scattering body.

The horizontal wind can be calculated from the cross-correlation function between signals received at different antennas, while the auto-correlation function determines the fading time of the echoes. These fading times characterize the irregular structure of the scatterer, which is usually caused by turbulence [14–16]. We use the horizontal wind speed data obtained by the cross-correlation function and the characteristic fading time data obtained by the auto-correlation function.

The relationship between the velocity fluctuations, V', caused by the random motion of the scatterer and the signal characteristic fading time, τ_c, can be expressed as [14]:

$$V' = \frac{\lambda\sqrt{\ln 2}}{4\pi\tau_c}, \quad (1)$$

where λ = 150.65 m is the radar wavelength. The energy per unit mass of this fluctuation is V'^2 [17]. The energy dissipation rate can be obtained by dividing the turbulent kinetic energy by a time scale. Assumed that the spectrum of the turbulent motions is inertial and that the vertical length scale will be limited by buoyancy, the Brunt–Väisälä period (also called buoyancy period) could be identified as a suitable timescale [18]. Weinstock [19] derived the following equation: $\epsilon = 0.4\sigma_z^2\omega_B$ (σ_z is the vertical velocity fluctuations and ω_B is the Brunt–Väisälä frequency), but did not discuss the effects of horizontal velocity fluctuations. Hall et al. [5,6] assumed a total velocity fluctuation, and thus, the total turbulence energy dissipation rate (ε_{total}) can be expressed as follows:

$$\varepsilon_{total} = cV'^2\omega_B. \tag{2}$$

The factor c is 0.8, which is related to the total velocity perturbation. As the signal may be affected by fluctuations in the buoyancy scale in the experiment and the estimate of ε only goes to the buoyancy scale, Equation (2) calculates an upper limit to the turbulent energy dissipation rate that can be obtained by this method.

When the scale of turbulence generation is comparable to the scale of viscous forces, turbulence generation will be suppressed and the kinematic viscosity will approach the turbulent diffusivity, so there will be a minimum value of the turbulence energy dissipation rate (ε_{min}) [5,6]:

$$\varepsilon_{min} = \upsilon\omega_B^2/\beta, \tag{3}$$

where υ is the kinematic viscosity, which is inversely proportional to the atmospheric density, and β is called the mixing coefficient representing the ratio of potential energy to kinetic energy dissipation [20]. The generally used approximation is $\beta = R_f/(1 - R_f)$, where R_f is the flux Richardson number. Lilly et al. [21] used $R_f = 1/4$ and obtained $\beta = 1/3 \approx 0.3$, which is generally accepted [5,6,22,23], so we use the same parameters. Because of a lack of atmospheric temperature and density data, we use NRLMSIS 2.0, an empirical atmospheric model [24], and calculate buoyancy frequency and kinematic viscosity. The actual measured data will make the calculations more accurate.

The actual energy dissipation rate can be accessed by subtracting the dissipation rate corresponding to the viscosity from the radar-derived total dissipation:

$$\varepsilon = \varepsilon_{total} - \varepsilon_{min}. \tag{4}$$

The turbopause is located as the height at which $\varepsilon = 0$.

Figure 1 gives an example of a radar profile, which shows the different characteristic changes of ε_{total} and ε_{min}. It can be seen from Figure 1 that ε_{total} is more heavily influenced by the real-time atmosphere, while the ε_{min} generally increases exponentially with height. The Brunt–Väisälä frequency also varies with height, but the variation is relatively small and it is not the dominant ε.

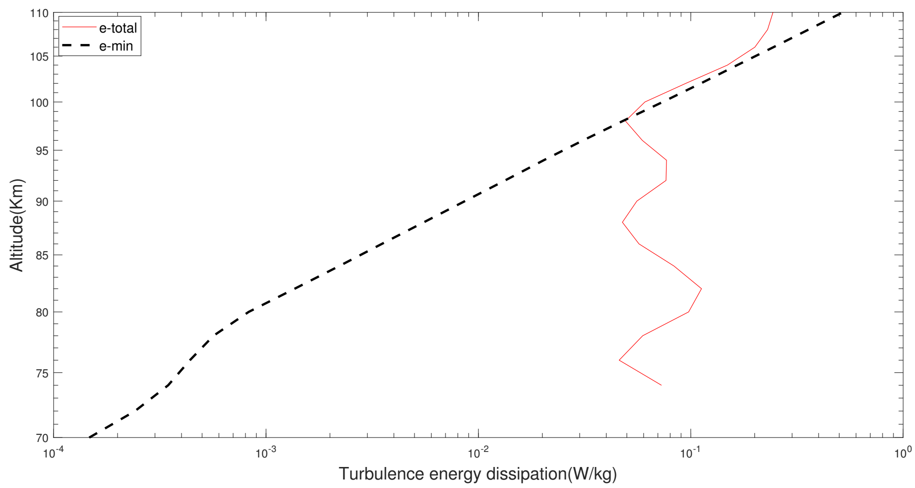

Figure 1. An example of the method for determining the turbopause. The red line represents ε_{total} and the black line represents ε_{min}. The position of the intersection of the two lines is the height of turbopause.

3. Results and Discussions

3.1. Short-Period Variation of ε in the MLT Region

The one-year variation in ε for different heights and the location of turbopause based on daily average data are illustrated in Figure 2. The daily average is averaged over a 24-h period and the radar will obtain about 360 profiles per day. There was a gap in the radar data for several days. The black line represents the turbopause, above which ε is negative (not shown in the figure). The altitude of the turbopause is obtained by linear interpolation. The regions of the greatest turbulence intensity are usually found to be 5–10 km below the turbopause, similar to the results of Hall et al. [5], with larger rates of turbulent energy dissipation sometimes present at lower heights. There are significant time-dependent variations in ε at different heights and locations of turbopause.

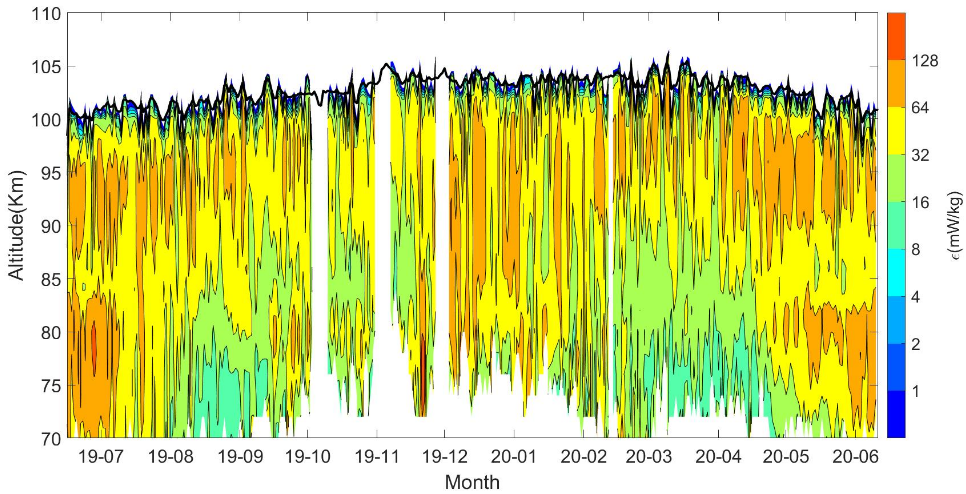

Figure 2. Estimation of daily ε with seasonal and elevation changes. The black line shows the results of a 5-day Gaussian smoothing process for the position where ε is zero, which is identified as the turbopause. The altitude of the turbopause is obtained by linear interpolation.

There are three distinct regions in Figure 2: the lower altitude (76–80 km), where both larger and smaller values of ε are usually observed, the middle altitude (84–88 km), where ε is relatively constant, and the region of maximum turbulence energy dissipation rate (94–98 km), where the maximum turbulence energy dissipation rate over the whole altitude usually occurs, and above which ε decreases rapidly. The turbulence energy dissipation rate for different regions is shown in Figure 3.

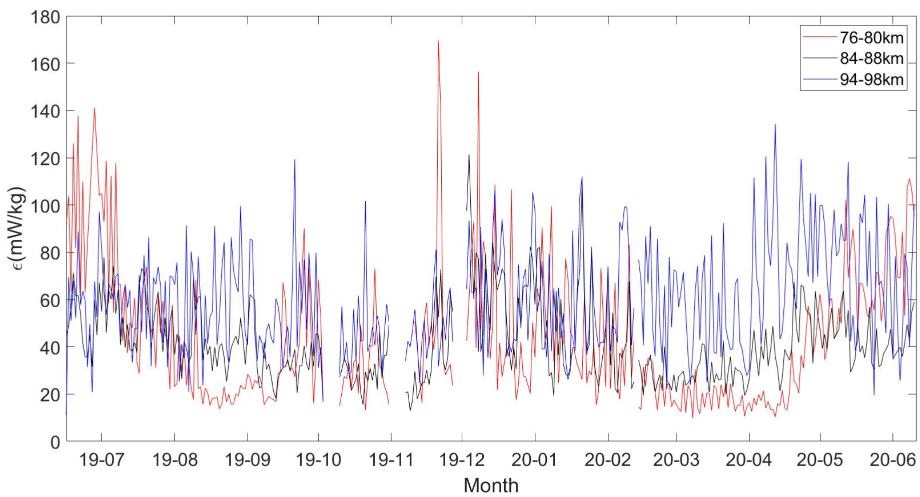

Figure 3. Estimation of daily ε for 76–80 km (red line), 84–88 km (black line), and 94–98 km (blue line).

As seen in Figure 3, at 76–80 km, there is an obvious semi-annual cycle in ε, with larger peaks occurring around July and December, sometimes exceeding those at 94–98 km. Holdsworth et al. [4] also observed that turbulent velocity have similar changes with equinoctial minima and solstice maxima value below 80 km. At 84–88 km, there is also an approximately semi-annual periodic variation in ε, but the variation is smaller in comparison and not synchronous with the variation at 76–80 km. Furthermore, at 94–98 km, there is no obvious semi-annual variation.

In order to study the short period variation of ε, ε at different regions and the altitude of the turbopause are hourly averaged and the time series are analyzed using Lomb–Scargle periodograms. The results are presented in Figure 4.

As can be seen in Figure 4, turbulence energy dissipation rate is modulated by the different periods, which are characteristic of the tides. At 76–80 km, ε has various periods. The most obvious one is the 24 h (24 h) periodic variation, followed by the 12 h (12 h) periodic variation, and it also has 8 h (8 h) periodic variation. At 84–88 km, as at 76–80 km, the most obvious periods of variation of ε are 24 h and 12 h, while the variation of other periods of ε is relatively small. At 94–98 km, the main periods of ε are 8 h, 12 h and 24 h, and unlike 76–80 km and 84–88 km, the most obvious period at 94–98 km is 12 h, and the 24 h periodic variation is relatively the least obvious. It can be seen that the 24 h period variation gradually loses its dominance as the height increases.

The turbopause is defined as the region in which the transition between turbulent mixing and molecular diffusion happens. Above the turbopause, mixing mechanism is dominated by molecular motion because the kinematic viscosity is so large that the turbulent motion is dampened. Below the turbopause, it is dominated by turbulence diffusion. The turbopause is occasionally considered to be the homopause, because at this height, the distribution of atmospheric components becomes different. Below this height, the atmospheric components are uniformly distributed by turbulent mixing, while above this height, the vertical distribution of the neutral components is related to their respective relative molecular masses. The height of the turbopause is a key parameter in many atmosphere models [24].

The period of variation of altitude of turbopause is similar with the 84–88 km ε, with the most pronounced 24 h periodic variation, followed by the 12 h periodic variation. Yuan et al. [25] noted very different diurnal tidal behavior in the upper middle atmosphere and in the region above turbopause.

In Figure 4, the 24 h change of ε loses its dominant position with the increase of altitude, which may be related to the propagation of diurnal tides in the atmosphere. Holdsworth et al. [4] pointed that the mechanism that produces the enhanced turbulence velocity may vary above and below 94 km and the large turbulent velocities were observed above 94 km, which is consistent with our result about the region where ε is the highest in Figure 2. This may explain the difference in the behavior of ε with a 12 h dominating period above 94 km and a 24 h dominating period below 94 km. At 94–98 km, the enhanced turbulence appears to be generated by diurnal tide breaks.

On the other hand, She et al. [26] noted that semi-diurnal tidal amplitudes can increase consistently to 100 km or more, which is consistent with the results of our harmonics analysis of tides. Semi-diurnal tides with longer vertical wavelengths suffer much less dissipation than diurnal tides with shorter vertical wavelengths saturated at lower altitudes. This may indicate that the semi-diurnal tide can propagate to higher positions, and therefore, ε is more influenced by it in higher altitude regions.

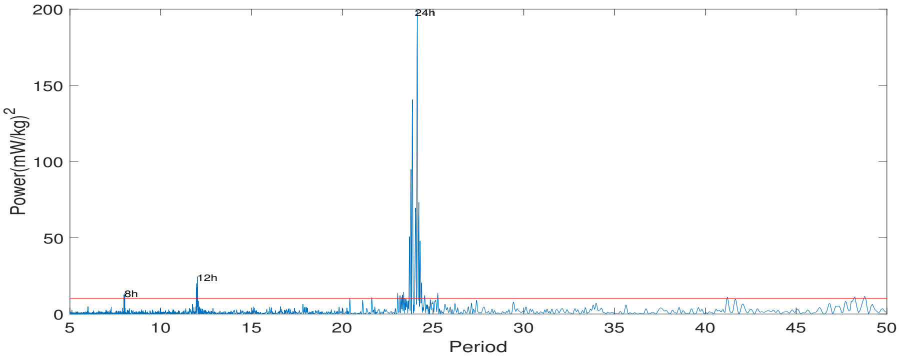

(**a**)

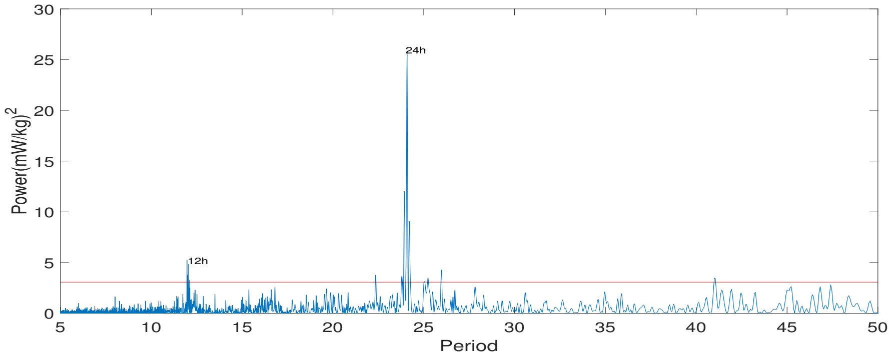

(**b**)

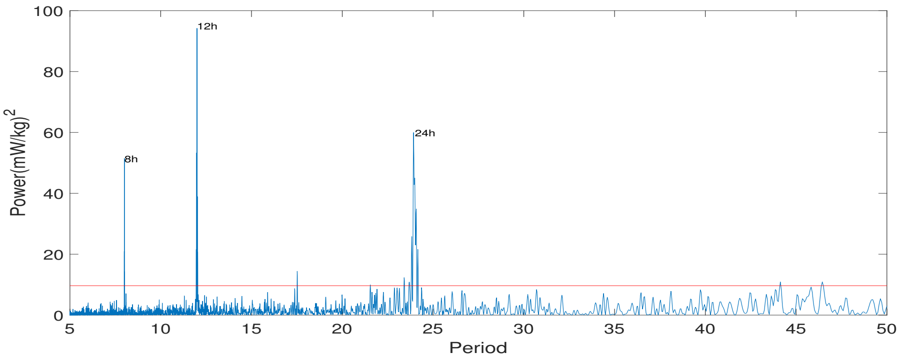

(**c**)

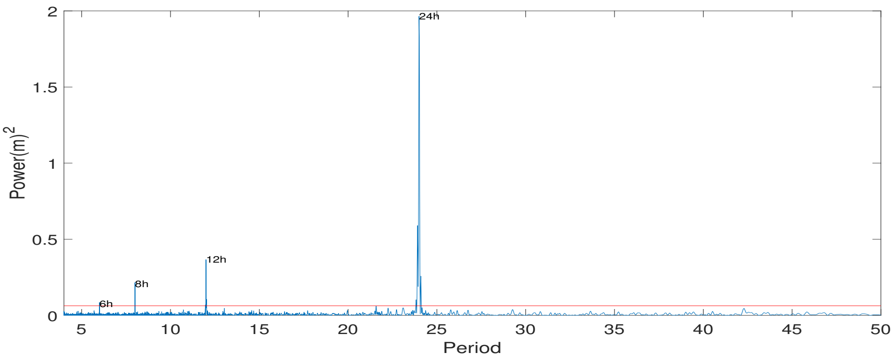

(**d**)

Figure 4. Lomb-Scargle periodograms for (**a**) 76–80 km; (**b**) 84–88 km; (**c**) 94–98 km ε. (**d**) The altitude of the turbopause. The red line represents a confidence level of 99%.

3.2. Relationship between the Activities of Atmospheric Turbulence and Atmospheric Tides

In order to analyze the relationship between the activities of atmospheric turbulence and atmospheric tidal wave, Lomb–Scargle periodograms are used for ε and the atmospheric total horizontal wind speed, and the results are presented in Figure 5.

At 76–80 km, ε and the atmospheric total horizontal wind speed have strong 24 h period activity in different months, as well as strong 12 h period activity in some months. Furthermore, they are more heavily split in the 24 h period, which may be due to the insufficient data. Furthermore, the relationship between the two at different periods is not that obvious.

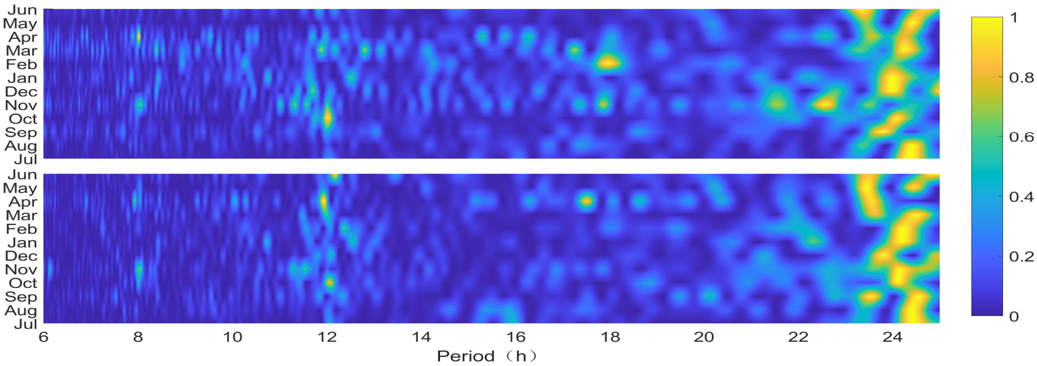

(**a**)

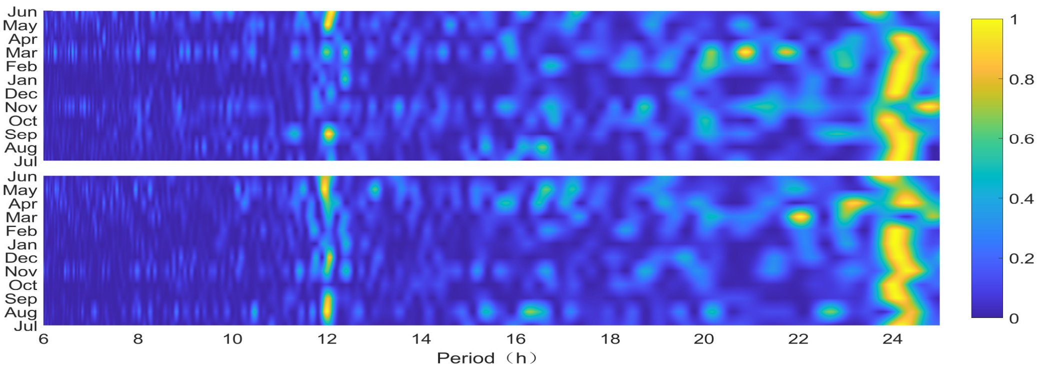

(**b**)

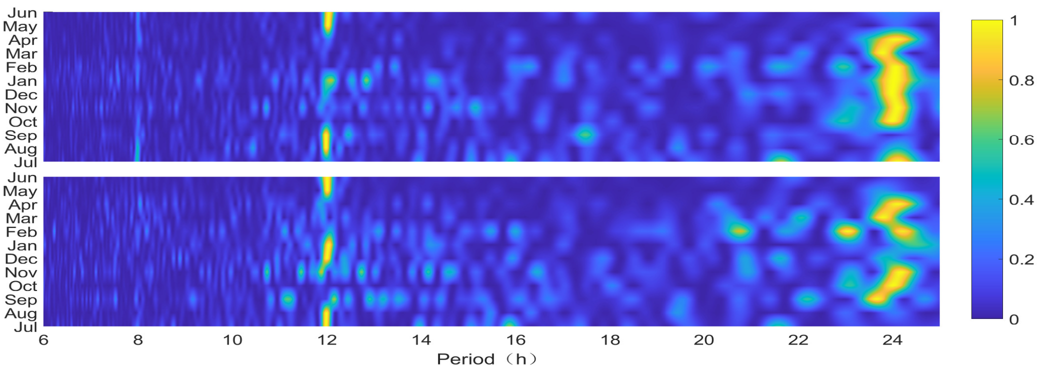

(**c**)

Figure 5. Normalized Lomb–Scargle periodograms for (**a**) 76–80 km, (**b**) 84–88 km, and (**c**) 94–98 km, with the turbulence energy dissipation rate and total horizontal wind speed in different months. Each graph displays the turbulence energy dissipation rate at the top and total horizontal wind speed below.

At 84–88 km,ε and the atmospheric total horizontal wind speed also have strong 24 h periods in different months, as well as strong 12 h periods in summer. At the same time, it can be seen that the corresponding relationship between the two is obvious in the 24 h and 12 h period.

At 94–98 km, for the total horizontal wind speed, 12 h period and 24 h period alternate with different months as the main period. For ε, 12 h period is the main activity period in summer and winter, while the 24 h period is the main activity period, except in August and September 2019 and May and June 2020. In summer, the 8 h period activity becomes apparent. Furthermore, the 12 h correspondence is more obvious than the 24 h correspondence. The value of the turbulent energy dissipation rate is also larger at this height, while the daily tide does not dominate, suggesting that the source of the turbulent energy dissipation rate may be the daily tide.

Meanwhile, some non-tidal periods may occur at different altitudes in some months, which may be caused by the coupling of tidal waves with other waves. For example, the 22 h period activity in April 2020 at 84–88 km may be caused by the coupling of 24 h tides and 6.5 day planetary waves. This may indicate that atmospheric turbulent activity is also influenced by some larger-scale waves.

It can be seen from Figure 5 that the 12 h period gradually replaces the 24 h period as the primary activity period as the height increases. The 24 h tidal component and 12 h tidal component of the horizontal wind speed and ε can be extracted by harmonic analysis. Compared with 84–88 km, the amplitude of ε increases slightly at 94–98 km in the 24 h period, while the amplitude of ε increases significantly at 94–98 km in the 12 h period. This also corresponds to a larger amplitude of the 12 h tidal component at higher altitudes for the total horizontal wind speed. These results show that ε is associated with tides. Holdsworth et al. [4] observed a strong diurnal component of turbulence velocity enhancement in the phase with the zonal wind component. During summer observations with the Scott Base MF radar (78° S, 167° E), Fraser and Khan [27] observed there to be a semidiurnal variation of the signal fading time (τ_c), and at 87–95 km, the minimum values of τ_c occur when the zonal component of the semidiurnal tide is at its westward maximum. Strelnikov [11] also noted that ε was modulated by 12 and 24 h.

The way tides modulate turbulence can be very complex: tides can modulate turbulence directly, tides breaking can generate turbulence [28], and tidal waves can even influence turbulence by modulating gravity waves [29].

Lindzen [28] argued that diurnal tidal wave breaking appears to be the main contributor to turbulent energy at tropical latitudes, while gravity wave breaking will dominate at middle and high latitudes. Furthermore, he shows that wave breaking appears to occur around 85 km, leading to a layer of enhanced eddy diffusion and wave-induced acceleration that extends between 85 km and about 108 km, with molecular transport dominating above this altitude. This is consistent with the height of turbopause calculated by us. Guo et al. [30] also found that the turbulence-induced temperature perturbations are strongest in the same altitude range where wave activity is most active, and weakest where the wave activity is the least active.

3.3. Relationship between the Activities of Atmospheric Turbulence and Atmospheric Gravity Waves

The 24 h and 12 h tidal components are found by harmonic analysis of the hourly average of total horizontal wind speed and ε. The prevailing winds and the 24 and 12 h tidal components were stripped of from the u (zonal) and v (meridional) data. The procedure gives a time series of u′, v′ perturbations, which are then split into 1-day segments and the gravity wave variance over the 20–120 min period range is calculated by integrating the power spectral density over the period range between 20 and 120 min [31]. Due to data limitations, we cannot effectively extract atmospheric wave parameters below 82 km, so we will concentrate on the region above 82 km.

It can be seen from Figure 6 that peaks of the activity of gravity wave and ε at different altitudes occurred in November and December 2019 and April and May 2020, which indicates that the activity of gravity wave and ε are related. Furthermore, the peaks at 94–98 km are not synchronized.

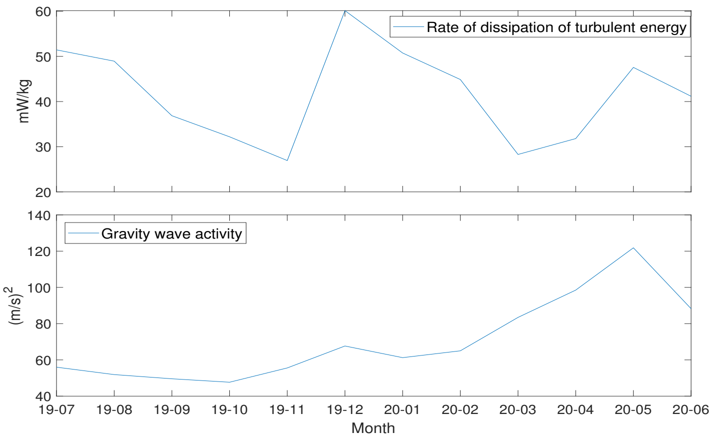

(**a**)

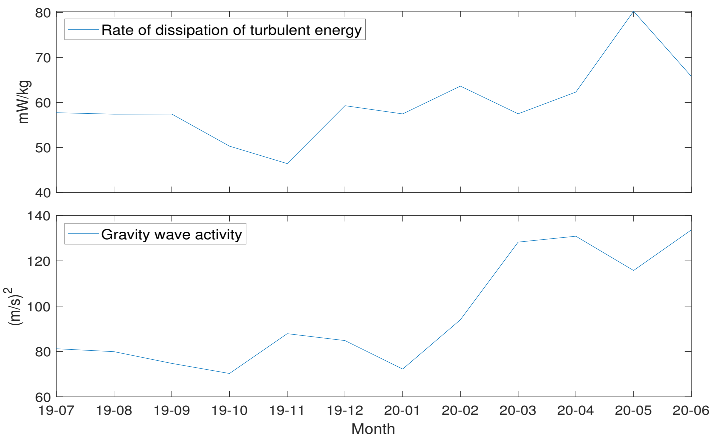

(**b**)

Figure 6. The ε value and the amplitude of the gravity wave with the monthly variation of (**a**) 84–88 km, (**b**) 94–98 km.

Turbulence energy dissipation rate has a semi-annual variation with solstice maxima, and the maximum value appeared in December and May 2019. The amplitude of gravity wave has a similar semi-annual maximum value variation. Our results about ε is consistent with the results of Kurosaki et al. [32] about the eddy diffusivity measured in the mesosphere over Shigaraki (35° N, 136° E). At the same site, similar variations in the activity of gravity wave were found by Tsuda et al. [33]. Furthermore, Sasi et al. [2] suggested that the observed enhancement of ε and vertical eddy diffusion coefficients during the summer monsoon season (June to September) may be associated with enhanced the activity of gravity wave over the Indian subcontinent at low latitudes. These observations support the hypothesis that turbulence is mainly generated by gravity waves breaking in the mesospheric region.

Gravity wave maximums generally occur in summer and winter, which may explain that the amplitudes of ε in different periods are also higher in summer and winter because of the influence of gravity waves. Furthermore, with respect to tides modulating gravity waves, Kinoshita et al. [29] showed the relationship between 1 and 4 h period gravity wave kinetic energy and latitudinal winds over 12 and 24 h. The results in Figures 5 and 6 indicate that gravity wave breaking and tide breaking may simultaneously have an effect on the generation of ε in the mid-latitude region.

With respect to gravity waves breaking into turbulence, Avsarkisov et al. [34] conducted a scaling analysis of three different dynamic states in the atmosphere: rotating stratified large turbulence (MST), stratified turbulence (ST), and small scale isotropic turbulence (KT). They suggested that the ST regime plays a significant role in the winter mesosphere region between 45 and 90 km and a secondary maximum of ST and KT above 90 km due to secondary gravity waves.

4. Conclusions

The atmospheric ε is modulated by different periods at different altitudes. The atmospheric ε is subject to 12 h and 24 h periodic variations at different altitudes. At higher altitudes, the 12 h periodic variation is more obvious than the 24 h periodic variation. The 12 h period gradually replaces the 24 h period as the primary activity period as the height increases. However, the periodic variation in the height of turbopause does not coincide with the region where ε is usually greatest, suggesting that there may be differences in the mechanisms affecting the two.

The activity of atmospheric turbulence is modulated by atmospheric tides, and the 12 h period correspondence is more pronounced than the 24 h period correspondence at higher altitudes. ε has a similar semi-annual maximum variation to the activity of gravity wave, which supports the hypothesis that the turbulence is generated by gravity wave breaking.

As the atmospheric density decays exponentially with height, the amplitude of the various atmospheric waves propagating vertically also increases rapidly, which can lead to saturation fragmentation and other instabilities. When waves propagate to a certain height, the breaking of the waves causes the momentum and energy of the large-scale waves to be transferred to the small and medium scales. This process then generates and enhances instability and turbulence. The difference in the behavior of ε above and below 90 km is significant, which may be due to the different sources of turbulent energy. Below 90 km, gravity wave breaking is the source of turbulent energy and also generates secondary gravity waves. The secondary gravity waves are a response to the localized momentum and thermal forcing associated with wave breaking. The source of turbulent energy above 90 km is mainly the breaking of daily tides and the breaking of secondary gravity waves.

Author Contributions: Conceptualization, C.X.; methodology, C.X. and Z.W.; software, Z.W.; validation, Z.W., C.X., X.H., J.Y., X.C. and Q.X.; formal analysis, Z.W.; investigation, C.X. and Z.W.; resources, X.H., J.Y., X.C. and Q.X.; data curation, X.H., J.Y., X.C. and Q.X.; writing—original draft preparation, Z.W.; writing—review and editing, Z.W., C.X., L.X. and X.W.; visualization, Z.W.; supervision, C.X.; project administration, C.X.; funding acquisition, C.X. All authors have read and agreed to the published version of the manuscript.

Funding: This research was funded by the National Natural Science Foundation of China (NSFC) Grant Nos. 91952111, 42174192, 12241101.

Institutional Review Board Statement: Not applicable.

Informed Consent Statement: Not applicable.

Data Availability Statement: If anyone is interested in the data used in the article, please contact the corresponding author.

Conflicts of Interest: The authors declare no conflict of interest.

References

1. Lübken, F.J. Seasonal variation of turbulent energy dissipation rates at high latitudes as determined by in situ measurements of neutral density fluctuations. *J. Geophys. Res.* **1997**, *102*, 13441–13456. [CrossRef]
2. Sasi, M.N.; Vijayan, L. Turbulence characteristics in the tropical mesosphere as obtained by MST radar at Gadanki (13.5° N, 79.2° E). *Ann. Geophys.* **2001**, *19*, 1019–1025. [CrossRef]
3. Roper, R.G.; Brosnahan, J.W. Diurnal variations in the rate of dissipation of turbulent energy in the equatorial upper mesosphere-lower thermosphere: Upper mesosphere turbulence. *Radio Sci.* **2005**, *40*, 1–15. [CrossRef]

4. Holdsworth, D.A.; Vincent, R.A.; Reid, I.M. Mesospheric turbulent velocity estimation using the Buckland Park MF radar. *Ann. Geophys.* **2001**, *19*, 1007–1017. [CrossRef]
5. Hall, C.M.; Meek, C.E.; Manson, A.H.; Nozawa, S. Turbopause determination, climatology, and climatic trends using medium frequency radars at 52° N and 70° N. *J. Geophys. Res.* **2008**, *113*, D13104. [CrossRef]
6. Hall, C.M.; Holmen, S.E.; Meek, C.E.; Manson, A.H.; Nozawa, S. Change in turbopause altitude at 52 and 70° N. *Atmos. Chem. Phys.* **2016**, *16*, 2299–2308. [CrossRef]
7. Lehmacher, G.A.; Larsen, M.F.; Collins, R.L.; Barjatya, A.; Strelnikov, B. On the short-term variability of turbulence and temperature in the winter mesosphere. *Ann. Geophys.* **2018**, *36*, 1099–1116. [CrossRef]
8. Li, J.; Collins, R.; Lu, X.; Williams, B. Lidar observations of instability and estimates of vertical eddy diffusivity induced by gravity wave breaking in the Arctic mesosphere. *JGR Atmos.* **2021**, *126*, e2020JD033450. [CrossRef]
9. Roper, R.; Berkey, F. Mesospheric and lower thermospheric turbulence over Bear Lake, Utah, 1999–2003. *J. Atmos.-Sol.-Terr. Phys.* **2011**, *73*, 921–924. [CrossRef]
10. Roper, R.G. Atmospheric turbulence in the meteor region. *J. Geophys. Res.* **1966**, *71*, 5785–5792. [CrossRef]
11. Strelnikov, B.; Szewczyk, A.; Strelnikova, I.; Latteck, R.; Baumgarten, G.; Lübken, F.J.; Rapp, M.; Fasoulas, S.; Löhle, S.; Eberhart, M.; et al. Spatial and temporal variability in MLT turbulence inferred from in situ and ground-based observations during the WADIS-1 sounding rocket campaign. *Ann. Geophys.* **2017**, *35*, 547–565. [CrossRef]
12. Cai, B.; Xu, Q.; Hu, X.; Yang, J. Initial Results of Meteor Wind with Langfang Medium Frequency Radar. *Atmosphere* **2020**, *11*, 507. [CrossRef]
13. Cai, B.; Xu, Q.; Hu, X.; Cheng, X.; Yang, J.; Li, W. Analysis of the correlation between horizontal wind and 11-year solar activity over Langfang, China. *Earth Planet. Phys.* **2021**, *5*, 270–279. [CrossRef]
14. Briggs, B. Radar observations of atmospheric winds and turbulence: A comparison of techniques. *J. Atmos. Terr. Sci.* **1980**, *42*, 823–833. [CrossRef]
15. Holdsworth, D.A.; Reid, I.M. A simple model of atmospheric radar backscatter: Description and application to the full correlation analysis of spaced antenna data. *Radio Sci.* **1995**, *30*, 1263–1280. [CrossRef]
16. Hocking, W.K. Strengths and limitations of MST radar measurements of middle-atmosphere winds. *Ann. Geophys.* **1997**, *15*, 1111–1122. [CrossRef]
17. Blamont, J.E. Turbulence in atmospheric motions between 90 and 130 km of altitude. *Planet Space Sci.* **1963**, *10*, 89–101. [CrossRef]
18. Manson, A.H.; Meek, C.E. Gravity waves of short period (5–90 min), in the lower thermosphere at 52 N (Saskatoon, Canada). *J. Atmos. Terr. Sci.* **1980**, *42*, 103–113. [CrossRef]
19. Weinstock, J. Energy Dissipation Rates of Turbulence in the Stable Free Atmosphere. *J. Atmos. Sci.* **1981**, *38*, 880–883. [CrossRef]
20. Oakey, N.S. Determination of the Rate of Dissipation of Turbulent Energy from Simultaneous Temperature and Velocity Shear Microstructure Measurements. *J. Phys. Oceanogr.* **1982**, *12*, 256–271. [CrossRef]
21. Lilly, D.K.; Waco, D.E.; Adelfang, S.I. Stratospheric Mixing Estimated from High-Altitude Turbulence Measurements. *J. Appl. Meteor.* **1974**, *13*, 488–493. [CrossRef]
22. Hocking, W.K. The dynamical parameters of turbulence theory as they apply to middle atmosphere studies. *Earth Planets Space* **1999**, *51*, 525–541. [CrossRef]
23. Gavrilov, N.M.; Luce, H.; Crochet, M.; Dalaudier, F.; Fukao, S. Turbulence parameter estimations from high-resolution balloon temperature measurements of the MUTSI-2000 campaign. *Ann. Geophys.* **2005**, *23*, 2401–2413. [CrossRef]
24. Emmert, J.T.; Drob, D.P.; Picone, J.M.; Siskind, D.E.; Jones, M.; Mlynczak, M.G.; Bernath, P.F.; Chu, X.; Doornbos, E.; Funke, B.; et al. NRLMSIS 2.0: A whole-atmosphere empirical model of temperature and neutral species densities. *Earth Space Sci.* **2021**, *8*, e2020EA001321. [CrossRef]
25. Yuan, T.; Stevens, M.H.; Englert, C.R.; Immel, T.J. Temperature tides across the mid-latitude summer turbopause measured by a sodium lidar and MIGHTI/ICON. *JGR Atmos.* **2021**, *126*, e2021JD035321. [CrossRef]
26. She, C.Y.; Krueger, D.A.; Yuan, T.; Oberheide, J. On the polarization relations of diurnal and semidiurnal tide in the mesopause region. *J. Atmos. Solar-Terr. Phys.* **2016**, *142*, 60–71. [CrossRef]
27. Fraser, G.J.; Khan, U. Semidiurnal variations in the time scale of irregularities near the Antarctic summer mesopause. *Radio Sci.* **1990**, *25*, 997–1003. [CrossRef]
28. Lindzen, R.S. Turbulence and stress owing to gravity wave and tidal breakdown. *J. Geophys. Res.* **1981**, *86*, 9707. [CrossRef]
29. Kinoshita, T.; Murayama, Y.; Kawamura, S. Tidal modulations of mesospheric gravity wave kinetic energy observed with MF radar at Poker Flat Research Range, Alaska. *J. Geophys. Res. Atmos.* **2015**, *120*, 6379–6390. [CrossRef]
30. Guo, Y.; Liu, A.Z.; Gardner, C.S. First Na lidar measurements of turbulence heat flux, thermal diffusivity, and energy dissipation rate in the mesopause region. *Geophys. Res. Lett.* **2017**, *44*, 5782–5790. [CrossRef]
31. Kovalam, S.; Tsuda, T.; Gurubaran, S. High-frequency gravity waves observed in the low-latitude mesosphere-lower thermosphere (MLT) region and their possible relationship to lower-atmospheric convection. *J. Geophys. Res.* **2011**, *116*, D15101. [CrossRef]
32. Kurosaki, S.; Yamanaka, M.; Hashiguchi, H.; Sato, T.; Fukao, S. Vertical eddy diffusivity in the lower and middle atmosphere: A climatology based on the MU radar observations during 1986–1992. *J. Atmos. Terr. Phys.* **1996**, *58*, 727–734. [CrossRef]

33. Tsuda, T.; Murayama, Y.; Yamamoto, M.; Kato, S.; Fukao, S. Seasonal variation of momentum flux in the mesosphere observed with the MU radar. *Geophys. Res. Lett.* **1990**, *17*, 725–728. [CrossRef]
34. Avsarkisov, V.; Becker, E.; Renkwitz, T. Turbulent Parameters in the Middle Atmosphere: Theoretical Estimates Deduced from a Gravity Wave–Resolving General Circulation Model. *J. Atmos. Sci.* **2022**, *79*, 933–952. [CrossRef]